

An Ultra-Wideband Janus Metastructure with Graphene for Detector Based on Anapole Mode in the Terahertz Region

Si-ying Li, Zhao Tang, Yang Cheng, and Hai-feng Zhang*

In this paper, an ultra-wideband Janus metastructure (MS) utilizing anapole mode for detector in the terahertz (THz) range by graphene is proposed. Specifically, when Fermi level (E_f) is set to 0.9 eV, the MS demonstrates ultra-broadband absorption exceeding 0.9 from 0.754 to 5 THz in the $-z$ -direction with a relative bandwidth of 147.6 %, in which perfect absorption of over 98% develops from 3.24 to 5 THz. In the case of the $+z$ -direction, the absorptivity maintains around 0.6 within the 0.745 ~ 5 THz range. As E_f equals 0 eV, the difference in absorption between the $-z$ -direction and $+z$ -direction exceeds 0.9 from 4.49 to 4.76 THz. The study also explores the MS for refractive index sensing near 3.71 THz by a unique difference detection, measuring two refractive index ranges: 1.2 ~ 2.6 and 4.5 ~ 4.7, with corresponding sensitivities of 0.0450 and 0.0304, respectively. Owing to its highly symmetrical structure, the MS is insensitive to the polarization state of the electromagnetic (EM) waves, performing remarkable angular stability as the incident angle varies from 0 to 60 degrees in the $-z$ -direction. These splendid properties make the design a good candidate for biomedical sensing, EM cloaking, and full-space EM wave control.

the localized enhancement of incident EM waves at subwavelength scales, MSs effectively enhance the sensitivity (S) of sensing. However, conventional metal-based THz MS detectors possess fixed EM characteristics after fabrication and are limited to specific frequencies.^[16,17] Consequently, researchers have extensively explored tunable materials, in which graphene is definitely a preferable choice.

Graphene, a two-dimensional honeycomb-like structure, displays semimetallic properties in the mid-infrared and THz range,^[18,19] enabling surface plasmon resonance within this frequency range.^[20] Due to its exceptional peculiarities such as low propagation loss, strong field confinement, and electrical tunability compared to metals, graphene has been widely employed in the design of current THz sensors. To name but a

1. Introduction

Terahertz (THz) waves, falling within the electromagnetic (EM) spectrum, span wavelengths from 0.03 to 3 mm.^[1,2] Positioned between microwaves and infrared waves, THz waves occupy a transitional region bridging electronics and photonics.^[3] With their transient nature,^[4] coherence,^[5] and excellent penetration capabilities,^[6,7] THz waves find diverse applications in biomedicine,^[8] security detection,^[9–12] and information communication,^[13] thus rendering them of significant research value.


Metastructures (MSs) are artificially designed subwavelength periodic composite materials that exhibit distinctive EM properties,^[14,15] including negative refractive index, EM-induced transparency, and perfect absorption. The development of MSs open up new opportunities for THz biosensing. By leveraging

few, in 2018, Chen et al. devised a three-dimensional graphene sensor capable of achieving perfect absorption across multiple frequency bands,^[21] while Zhang et al. proposed a three-band THz sensor by graphene.^[22] Nevertheless, they do not have the excellent feature of wide absorption band width.

And the anapole mode, initially introduced by Zel'dovich in 1958 can substantially enhance the absorption and has gained recognition in nuclear, molecular, and atomic physics.^[23,24] It can be represented as a polar current flowing on the surface of a circular ring, generating a concentrated static magnetic field confined within the ring as well as possessing disruptive interference traits between toroidal dipole moments (T) and electric dipole moments (P). However, in the published academic research on the anapole, most of the absorption and relative absorption bandwidth ($RABW$) are not ideal. In 2021, Guo et al. introduced an anapole mode-based MS operating in the THz band with an absorption rate of less than 90 %.^[25] Thus the design of ultra-wideband absorption applying anapole mode needs to be solved urgently.

In addition, most current MSs function solely in either pure reflection mode or pure transmission mode, leaving a significant portion of the EM spectrum unexplored. The concept of Janus materials originated from a lecture by P. G. Gennes and has since been embraced by the scientific community to describe materials that possess distinct properties on opposing sides or surfaces.^[26] Over the past thirty years, a multitude of Janus materials have

S.-ying Li, Z. Tang, Y. Cheng, H.-feng Zhang
College of Electronic and Optical Engineering & College of Flexible
Electronics (Future Technology)
Nanjing University of Posts and Telecommunications
Nanjing 210023, P. R. China
E-mail: hanlor@njupt.edu.cn

 The ORCID identification number(s) for the author(s) of this article can be found under <https://doi.org/10.1002/andp.202300244>

DOI: 10.1002/andp.202300244

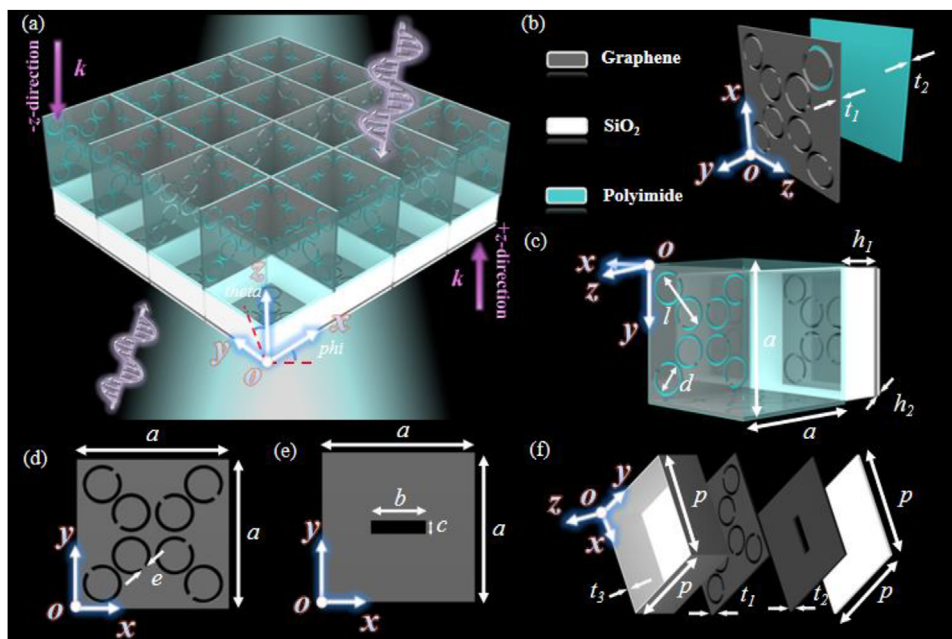


Figure 1. Schematic diagrams of the MS, a) the periodic array of the design, b) the left side unfolding view of the first layer of the design, c) unit structure diagram, d,e) top views of the ORGS and RSG with dimensional parameters, f) the intermediate structure unfolding view of the MS.

been developed, leading to a wide range of new applications in macro/microstructures,^[27,28] including sensors,^[29] cellular, drug encapsulation,^[30,31] and bionic interfaces.^[32–34] It is important to highlight that by introducing Janus properties, the capabilities of MSs in controlling EM waves are enormously expanded, thus stimulating the exploration of high-performance multifunctional devices capable of meeting more demanding and diverse application requirements.^[35–37]

In contrast to existing work,^[38–40] this study presents a novel Janus MS detector based on anapole mode with highly efficient absorption in the THz range, achieved by leveraging the tunable properties of graphene. The MS exhibits distinct frequency-selective effects in the forward ($-z$) and backward ($+z$) propagation directions. Through control of the Fermi level (E_f) of graphene, the absorption asymmetry between the forward and backward directions can be dynamically modulated. Specifically, when E_f is set to 0.9 eV, the proposed MS demonstrates ultra-broadband absorption in the $-z$ -direction (A_-) exceeding 0.9 from 0.754 to 5 THz with a RABW of 147.6 %, in which perfect absorption of over 98% develops from 3.24 to 5 THz. While the absorption in the $+z$ -direction (A_+) remains around 0.6 within the 0.754 ~ 5 THz range, indicating a significant difference in absorption between the forward and backward directions ($\Delta A = A_- - A_+$). When E_f is 0 eV, corresponding to zero external voltage, the nonreciprocity becomes more pronounced. Particularly noteworthy is the frequency range of 4.49 to 4.76 THz, where the ΔA exceeds 0.9. Leveraging the differential absorption properties resulting from the anapole mode and toroidal dipole modes, the study explores the potential for refractive index sensing near 3.71 THz, where E_f equals 0 eV. It is discovered that the MS can measure refractive index (n) within two ranges: 1.2 ~ 2.6 and 4.5 ~ 4.7, with corresponding S of 0.125 THz/RIU (S_1) ($S_2 = 0.0450$)

and 0.094 THz/RIU (S_1) ($S_2 = 0.0304$). Additionally, the study discusses relevant structural parameter and the absorption property of the structure at different incident angles (θ) (defined as the angle in the γoz plane between the incident EM waves and the positive direction of z -axis) and polarization angles (ϕ) (defined as the angle in the xoy plane between the incident EM waves and the positive direction of x -axis). Notably, in the transverse magnetic (TM) mode (the electric field aligns with the x -axis, the magnetic field aligns with the γ -axis, and the wave vector aligns with the z -axis), the MS exhibits remarkable angular stability as the θ varies from 0 to 60 degrees in the $-z$ -direction. This design holds significant potential for applications in biomedical sensing, radar stealth technology, and full-space EM wave control.

2. Design and Simulations

2.1. Theoretical Simulation of the Design

Figure 1a illustrates the periodic array diagram of the MS. The terms “ $-z$ -direction” and “ $+z$ -direction” refer to the direction of the wavevector (k -direction). The unit cell structure is depicted in Figure 1c, where the open-ring graphene structure on the side (ORGS) is shown in Figure 1d. The ORGS, with a thickness of t_1 , is positioned on a dielectric substrate with a thickness of t_2 , as depicted in Figure 1b. The dielectric substrate material is polyimide, which has a relative permittivity of 3.5 and a loss tangent of 0.03.^[41] To obtain Figure 1f, the intermediate structure in Figure 1c is unfolded, resulting in two containers made of silicon dioxide with a relative permittivity of 1, serving as the host for the analyte. The gap between the two containers is formed by the open-ring graphene structure in the middle (ORGM) and rectangular slits graphene

Table 1. The detailed parameters.

Parameter	<i>a</i>	<i>b</i>	<i>C</i>	<i>d</i>	<i>e</i>	<i>l</i>
Value [μm]	110	40	10	24	4	26
Parameter	<i>p</i>	<i>h</i> ₁	<i>h</i> ₂	<i>t</i> ₁	<i>t</i> ₂	<i>t</i> ₃
Value [μm]	110	45	3	2.5	0.5	3

(RSG), aiming to enhance absorption. And the absorption rate is calculated using the following formula:^[42]

$$A(\omega) = 1 - R(\omega) - T_z(\omega) - P(\omega) \quad (1)$$

where the reflectance is represented by $R(\omega) = |S_{11}|^2$, while the transmittance is denoted by $T_z(\omega) = |S_{21}|^2$. Meanwhile, $P(\omega)$ indicates the polarization conversion efficiency.

The central ORGM is identical to the side ORGS structure, as illustrated in Figure 1e. The other detailed parameters can be found in Table 1.

The dynamic surface conductivity of graphene in the THz range, denoted as $\sigma_g(\omega)$, can be determined by applying the Kubo formula.^[44] The surface conductivity $\sigma_g(\omega)$ of graphene consists of two distinct components: the intraband conductivity, $\sigma_{\text{intra}}(\omega)$ and the interband conductivity, $\sigma_{\text{inter}}(\omega)$.^[43]

$$\sigma_g(\omega) = \sigma_{\text{intra}} + \sigma_{\text{inter}} \quad (2)$$

where $\sigma_{\text{intra}}(\omega)$, and $\sigma_{\text{inter}}(\omega)$, can be mathematically expressed by the following equations:^[43]

$$\sigma_{\text{intra}}(\omega) = \frac{-je^2 k_b T}{\pi \hbar^2 (\omega + 2j\tau)} \left(\frac{\mu_c}{k_b T} + 2 \ln(e^{\frac{\mu_c}{k_b T}} + 1) \right) \quad (3)$$

$$\sigma_{\text{inter}}(\omega) = \frac{-je^2}{4\pi \hbar} \ln \left(\frac{2\mu_c - (\omega + 2j\Gamma)\hbar}{2\mu_c + (\omega + 2j\Gamma)\hbar} \right) \quad (4)$$

The symbol ω represents the angular frequency of incident THz waves, e denotes the charge of an electron, k_b refers to the Boltzmann constant, and \hbar is the reduced Planck constant defined as $\hbar = h/(2\pi)$, where h is the Planck constant. Additionally, Γ and T correspond to 0.43 meV and 300 K,^[44] respectively, representing specific values for the interband scattering rate and temperature. In general, the interband conductivity of graphene can be disregarded,^[45] leading to the simplification of graphene's surface conductivity using the Drude model:^[43]

$$\sigma_g(\omega) \approx \frac{e^2 \mu_c}{\pi t^2} \frac{j}{\omega + j/\pi} \quad (5)$$

Thus, the surface conductivity of graphene can be adjusted by varying E_f . The relationship between the E_f of graphene and the applied bias voltage is given by the following equation:^[46]

$$\mu_c \approx \hbar V_f \sqrt{\frac{\pi \epsilon_0 \epsilon_r V_g}{et}} \quad (6)$$

where $V_f = 1.1 \times 10^6$ m/s is the Fermi velocity of graphene, t represents the thickness of the dielectric layer, and V_g is the applied

bias voltage. Additionally, ϵ_0 and ϵ_r denote the permittivity of the vacuum and the dielectric layer, respectively.

It is worth emphasizing that this work is theoretical in nature, and the experimental aspects are beyond the scope of our study. However, the data obtained from our simulations is reliable. With the aid of commercial EM simulation software, High-Frequency Structure Simulator (HFSS), we established the model and obtained the data results. In the simulations, periodic boundary conditions were set along the *x*- and *y*-axes, while spatial boundary conditions were set along the *z*-axis. The EM wave, polarized along the *x*-axis, was incident along the *z*-axis onto the MS. The proposed design can be fabricated, and the specific fabrication process can be found in the referenced literature.^[47–50] However, the structure is complex, and the accuracy of processing, tolerance, and temperature and pressure resistance need to be further considered.

Due to the perfect symmetry of the proposed MS, simulation results indicate that the effects are the same for both transverse electric (TE) mode (electric field along the *y*-axis, magnetic field along the *x*-axis, and wave vector along the *z*-axis) and TM mode. Therefore, the subsequent discussion will primarily focus on the TE mode.

2.2. The Mechanistic Analysis for Absorption

At an E_f value of 0.9 eV, graphene exhibits higher conductivity. In the proposed MS, the ring apertures are arranged along the diagonal. When vertically incident TE-polarized waves are present, the electric field aligns parallel to the *y*-axis. This excites oscillating charges that are perpendicular to the waist of the ring apertures. Consequently, a strong **P** pointing occurs in the direction perpendicular to the diagonal, as illustrated in Figure 2a. The oscillating charges induced by the incident EM waves give rise to two radial currents (**J**) that flow along the edges of the ring apertures, as indicated by the blue arrows. These opposing circulating currents generate two opposing magnetic dipole moments (**M**), labeled in purple. When the **M** are connected end-to-end, they form a **T** pointing in the direction perpendicular to the diagonal, described by the yellow arrows in Figure 2b.

The quantities **P**, **M**, and **T** can all be expressed in terms of the current density **J**.^[51]

$$\mathbf{P} = \frac{1}{i\omega} \int d^3 r \mathbf{J} \quad (7)$$

$$\mathbf{M} = \frac{1}{2c} \int [\mathbf{r} \times \mathbf{J}] d^3 r \quad (8)$$

$$\mathbf{T} = \frac{1}{10c} \int d^3 r [\mathbf{r}(\mathbf{r} \cdot \mathbf{J}) - 2\mathbf{J}r^2] \quad (9)$$

where k is the wave number, c is the speed of light, and r is the position vector.

Assuming that the toroidal dipole moment **T** and the electric dipole moment **P** are positioned at the origin ($r = 0$), the total

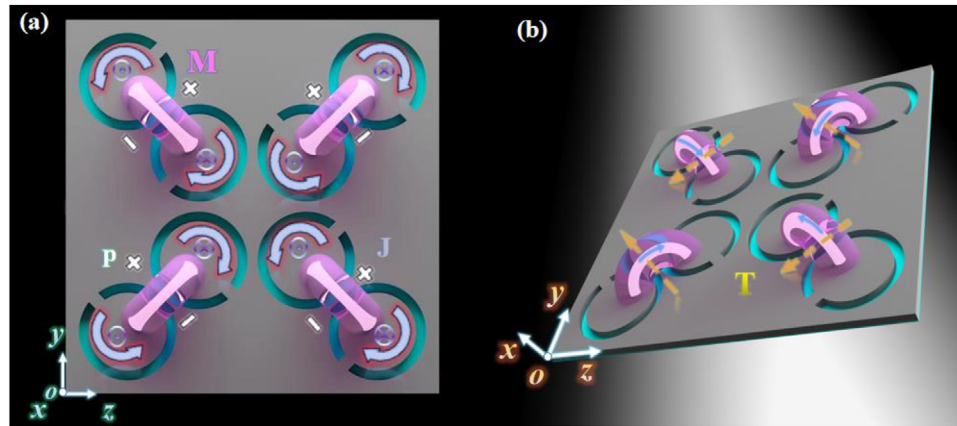


Figure 2. Schematic diagram of the formation principle of a) P, M, J, and b) T.

radiated electric field E_{total} and magnetic field H_{total} due to the superposition of the two dipoles are given by:^[51]

$$\mathbf{E}_{\text{total}} = \mathbf{E}_P + \mathbf{E}_T = \left[\frac{(\mathbf{r} \cdot (\mathbf{P} - ik\mathbf{T}))F(\omega, r)}{c^2 r^2} \mathbf{r} - \frac{G(\omega, r)}{c^2 r} (\mathbf{P} - ik\mathbf{T}) \right] \times \frac{\exp(-ikr + i\omega t)}{r} \quad (10)$$

$$\mathbf{H}_{\text{total}} = \mathbf{H}_P + \mathbf{H}_T = -\frac{ikD(\omega, r)}{cr} [\mathbf{r} \times (\mathbf{P} - ik\mathbf{T})] \frac{\exp(-ikr + i\omega t)}{r} \quad (11)$$

It is worth noting that according to the equation, when $\mathbf{P} = ik\mathbf{T}$, anapole resonance occurs, and the superimposed electric and magnetic fields vanish in the far field. However, in the near field region ($r = 0$), a significant localization of EM energy occurs. The expressions for this localization can be shown as:^[51]

$$\mathbf{E}_{\text{total}}(r=0) = ikT\delta(r) \exp(i\omega t) \quad (12)$$

$$\mathbf{H}_{\text{total}}(r=0) = ikrot [\mathbf{T}\delta(r)] \exp(i\omega t) \quad (13)$$

During anapole resonance, the destructive interference of the P and T are brought about, at the same time inducing strong field enhancement.

The structure as a square cavity by cooperating ORGSs and dielectric substrates are introduced in our initial exploration. The EM characteristics of the structure are depicted in Figure 3a. The structure demonstrates absorption levels above 0.7 in the frequency range of 0.168 to 5 THz, with a peak absorption value of 0.932 observed at 3.485 THz. Under the influence of the external EM field, the far-field effects of the MS can be approximated as the response of electric/magnetic multipoles and toroidal multipoles. To gain further insight into the absorption mechanism, we analyzed the scattered energy of the multipole scattering powers (P, T, M, Qe, and Qm) as illustrated in Figure 3b. It can be observed that the scattering power of the toroidal dipole moment T

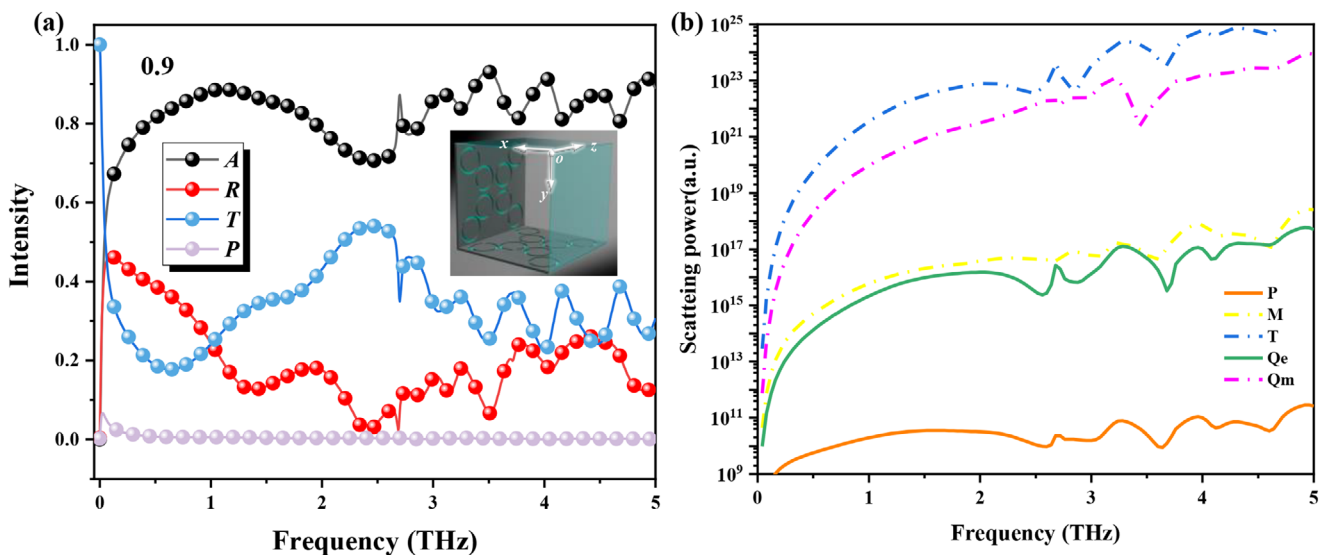


Figure 3. EM properties of the square cavity: a) Absorption (A), reflectance (R), transmittance (T), and polarization conversion (P) curves with frequency, b) multipole scattering power distribution.

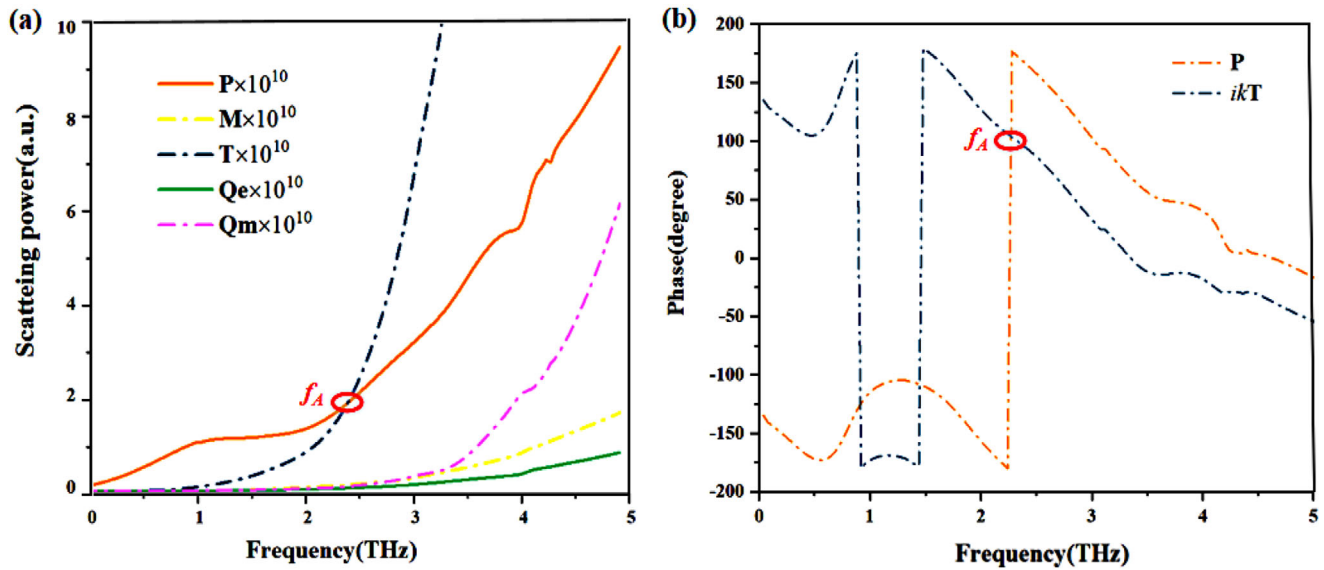


Figure 4. a) Contributions of P, M, T, Qe, and Qm and the amplitude of P and T are equal at $f_A = 2.30$ THz. b) Phases of P and ikT , where the phase difference of P and ikT achieve 0 at f_A .

is significantly larger than that of the other multipoles, indicating its dominant role in the absorption process of the structure.

To further enhance the difference between A_+ and A_- , we incorporated the ORGM and RSG in the middle of the square cavity. Based on the current distribution calculations, the multipole scattering powers and phases for the ORGM are obtained. Figure 4a shows that the scattering powers of P and T are considerably larger than those of other multipoles, demonstrating that P and T play a dominant role in the structure. At the frequency of 2.30 THz (f_A), when the incident EM wave is horizontally polarized, the scattering powers of the electric dipole moment P and the toroidal dipole moment T are equal, resulting in strong interference and inducing anapole resonance, leading to a significant localization of the EM wave.

With the aim of validating the mechanism and characteristics of the anapole resonance, simulations were performed to analyze the vector current and vector magnetic field distributions when the MS was vertically illuminated by TE waves at the frequency f_A , as shown in Figure 5. In Figure 5a, the electric field energy is predominantly localized around the ring apertures, consistent with the theoretical analysis mentioned above, thereby confirming the existence of the toroidal dipole moment T. Furthermore, when TE waves at the frequency f_A are vertically incident, the vector magnetic field inside the metasurface structure forms a loop as displayed in Figure 5b, which is a significant characteristic of the magnetic field distribution during anapole resonance, thus confirming the theoretical analysis presented earlier. The agreement between the simulation results and the theoretical analysis

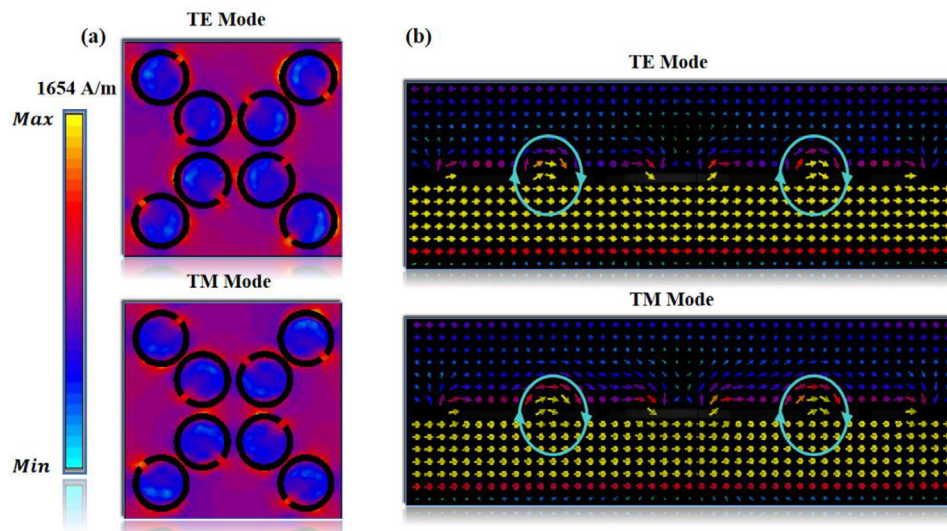


Figure 5. a) Surface current diagram of the ORGM at f_A , b) the magnetic field distribution at f_A cross-section along the diagonal $y = x$.

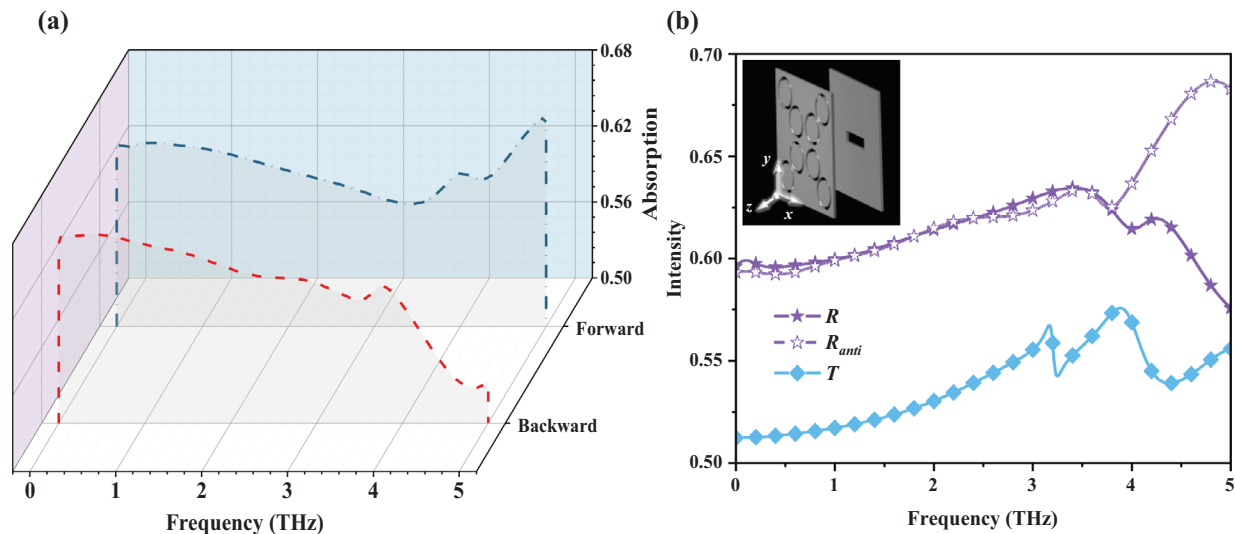


Figure 6. a) Absorption curves of the intermediate structures, b) the intensity of the R (forward reflection), R_{anti} (backward reflection), and T (transmission) of the intermediate structures.

provides strong evidence for the occurrence of anapole resonance in the proposed MS and validates its underlying mechanism.

According to the analysis of the simulation results, it was found that there was a substantial disparity in the absorption characteristics between the forward and backward directions when the middle structure was acting alone, as shown in **Figure 6a**. In **Figure 6b**, the maximum difference between forward reflection and backward reflection can reach 0.166.

By combining the middle structure with the square cavity, a highly desirable differential A_+ and A_- effect is achieved. As shown in **Figure 7a**, the structure achieves the A_+ above 0.9 in the frequency range of 0.754 ~ 5 THz with a RABW of 147.6 %, as well as a remarkable perfect absorption of 99.9% at 3.483 THz (f_1). When the EM wave is incident from the opposite direction, the absorption maintains around 0.6 in the range of 0 ~ 5 THz, and ΔA reaches its maximum value of 0.451 at 4.721 THz. In **Figure 7b**, it is evident that the forward reflection maintains a sustained level of around 0.6 in the frequency range of 0.5 to 5 THz, forming a high reflection window, while the forward reflection is roughly all below 0.2. And thanks to the addition of the intermediate structure, an ultra-low transmittance band with nearly 0 transmittance is formed. These results demonstrate the effectiveness of the proposed design in achieving highly efficient absorption and significant differentiation between forward and backward propagation directions, making it suitable for applications requiring tailored absorption properties and control of EM wave transmission.

For the sake of exploring the perfect absorption mechanism of the MS at the specific frequency point f_1 , the surface current distributions are analyzed. The results in **Figure 8** provide insights into the current flow and electric field localization. It can be observed that in the TE mode, the excitation occurs on the side and perpendicular to the y -axis of the annular graphene aperture, as depicted in **Figure 8a**. A significant amount of electric field is localized around the annular region, indicating a concentration of energy. In comparison, as shown in **Figure 8c**, there is a smaller current distribution on the ORGM, with the electric field mainly

concentrated at both ends of the y -axis. When it comes to the RSG in **Figure 8d**, the surface current is mainly distributed at the single slit and in the hollow area of the ORGM in front, while the current intensity is still smaller. In the TM mode, the excitation occurs on the side and perpendicular to the x -axis of the annular graphene aperture, as illustrated in **Figure 8b**. The electric field distribution in the middle structure is similar to that in the TE mode, exhibiting less localized electric field energy, distributed mainly at both ends of the x -axis. These observations provide further evidence of the localization of electric field energy and the role of specific components in the MS, contributing to the achievement of perfect absorption at the specific frequency point f_1 .

Leveraging the tunability of graphene, it has been discovered that as E_f varies from 0.9 eV to 0 eV, as described in **Figure 9**, the ΔA increases. In **Figure 9a**, the absorption in the forward direction remains relatively stable at a higher value across the range of E_f values considered. On the other hand, the absorption in the backward direction exhibits a decreasing trend as the E_f decreases, which is illustrated in **Figure 9b**. This implies that the MS becomes less effective in absorbing energy in the backward direction at lower E_f values. In particular, when E_f is 0 eV, as demonstrated in **Figure 7c**, the A_+ remains above 0.6 and achieves an absorption value of 0.987 at 3.71 THz. It can be observed from **Figure 7b** that the backward reflection maintains a higher value of above 0.8, while the forward reflection reaches a minimum value of 0.070. This significant contrast between forward and backward reflections confirms the achievement of a pronounced difference in absorption between the two directions. Notably, the structure exhibits three absorption bands above 0.9 in the forward direction (1.435 ~ 2.212 THz, 3.606 ~ 3.797 THz, 4.486 ~ 4.767 THz), among which the ΔA exceeds 0.9 in the frequency range of 4.49 ~ 4.76 THz, indicating a strong difference in the forward and backward absorption response of the MS.

The analysis of the surface current distribution at the perfect absorption point f_2 (3.71 THz) when E_f is 0 eV provides insights into the behavior of the design. In the TE mode, the incident

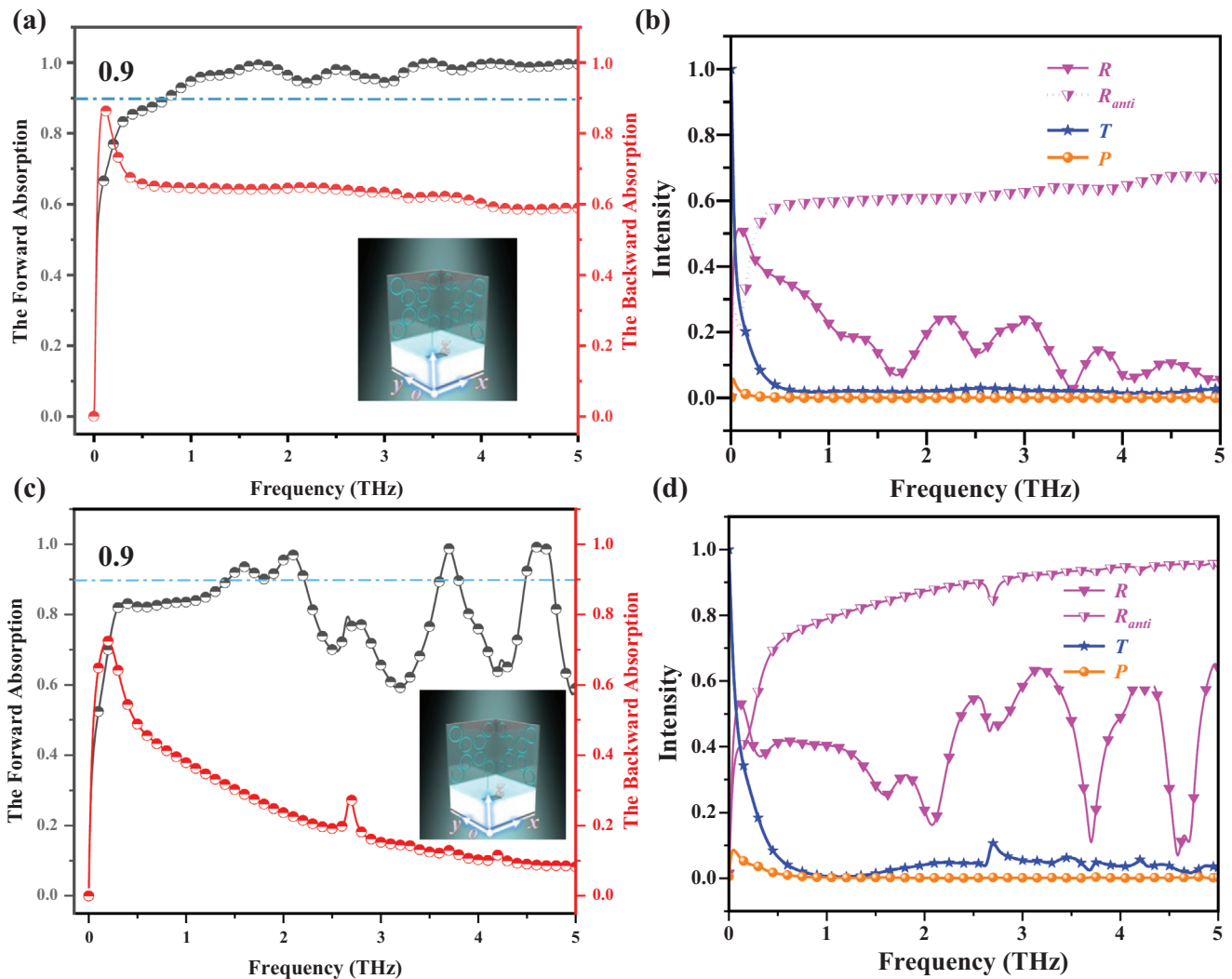


Figure 7. Absorption curves charts, a) $E_f = 0.9$ eV, c) $E_f = 0$ eV. The diagrams of the intensity of R , R_{anti} , T , b) $E_f = 0.9$ eV, d) $E_f = 0$ eV.

electric field wave excites the ORGS perpendicular to the y -axis, with the electric field primarily distributed in the upper half of the ORGS. Conversely, in the TM mode, the excitation mainly occurs on the right side of the ORGS, with the electric field predominantly localized in its left half. Interestingly, The ORGM in the middle structure exhibits relatively low absorption of electric field energy in both TE and TM modes, as shown in **Figure 10c**. This suggests that the ORGM is not the primary contributor to the absorption at the perfect absorption point f_2 . And the electric field energy is mainly localized at the single slit and the edge of the RSG in **Figure 10d**. Overall, the surface current distribution analysis provides further evidence of the absorption mechanism and highlights the specific regions where the electric field energy is localized, emphasizing the roles of the ORGS and RSG in achieving the perfect absorption response at f_2 in the TE mode.

In an effort to gain further insight into the energy flow within the MS and to highlight the differences between forward and backward incidence, we conducted an energy flow analysis by adding monitors. By analyzing the energy flow at cross-section

A (as shown in **Figure 11a**), validating the reasons behind the differences between A and A_+ can be fulfilled.

From **Figure 12a**, it can be observed that when $E_f = 0.9$ eV, at the perfect absorption point of 3.483 THz, a significant amount of EM waves from forward incidence is absorbed by the ORGS, then reflected by the middle structure, with only a small portion transmitting through. This results in excellent energy confinement. In the backward incidence case, the energy flow analysis shows a different pattern. a large amount of energy is transmitted through the ORGS but reflected by the middle structure, resulting in lower absorption in the backward direction, consistent with the previous analysis, as shown in **Figure 12c**. The energy flow lines indicate that a significant portion of the energy is trapped and circulates within the central region. When $E_f = 0$ eV, most of the forward incident EM waves are reflected at the absorption point of 3.71 THz by the middle structure, forming a circular energy flow near the side annular graphene aperture as well as indicating its strong localization effect on energy flow and achieving high absorption. On the contrary, when the EM waves are

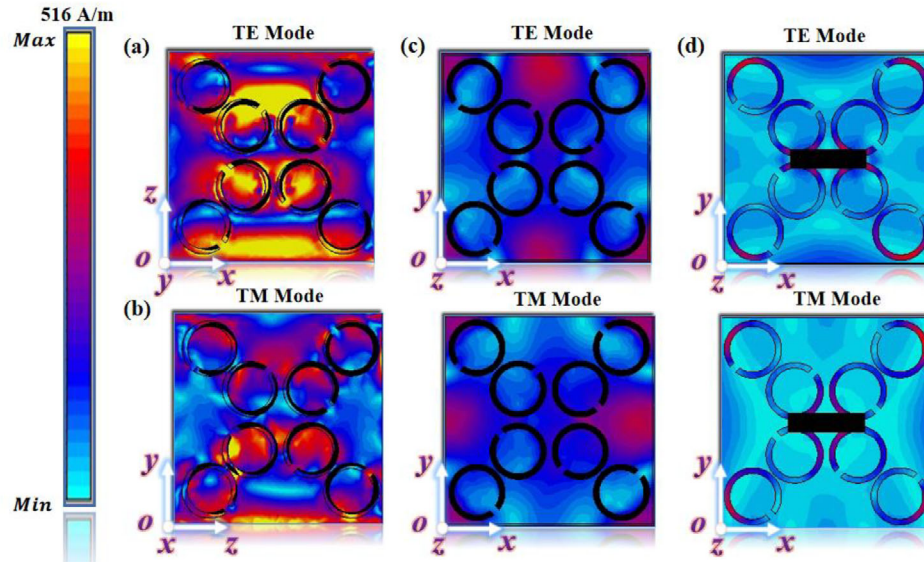


Figure 8. Surface current distributions of ($E_f = 0.9$ eV): a) the ORGS perpendicular to the y -axis at f_1 , b) the ORGS perpendicular to the x -axis at f_1 , c) the ORGM at f_1 , d) the RSG at f_1 .

backward incident, it is found that a significant portion of the energy can transmit through the middle structure, resulting in a sharp decrease in absorption.

Impedance matching theory provides a valuable framework for analyzing the EM absorption mechanism of the MS. When the MS approaches the absorption point, its equivalent surface impedance Z should be equal to the impedance Z_0 in free space, that is to say, normalized impedance $Z_r = Z/Z_0$ equals 1. When the EM waves are normally incident, the relationship between Z_r and absorption can be succinctly expressed as follows:^[47,48]

$$A(\omega) = 1 - R(\omega) - T_z(\omega) - P(\omega) = 1 - R(\omega) = 1 - \frac{|Z_r - 1|}{|Z_r + 1|} \quad (14)$$

where S_{11} and S_{21} represent the reflection coefficient and transmission coefficient, respectively, and they can be expressed as the following equations,^[52,53]

$$S_{11} = \frac{i}{2} \left(\frac{1}{z} - z \right) \sin(nkd) \quad (15)$$

$$S_{21} = \frac{1}{\cos(nkd) - \frac{i}{2} \left(\frac{1}{z} + z \right) \sin(nkd)} \quad (16)$$

According to Equation (14), the absorption efficiency $A(\omega)$ can reach its maximum value only when Z_r is close to 1. Utilizing impedance matching theory, we can further analyze and

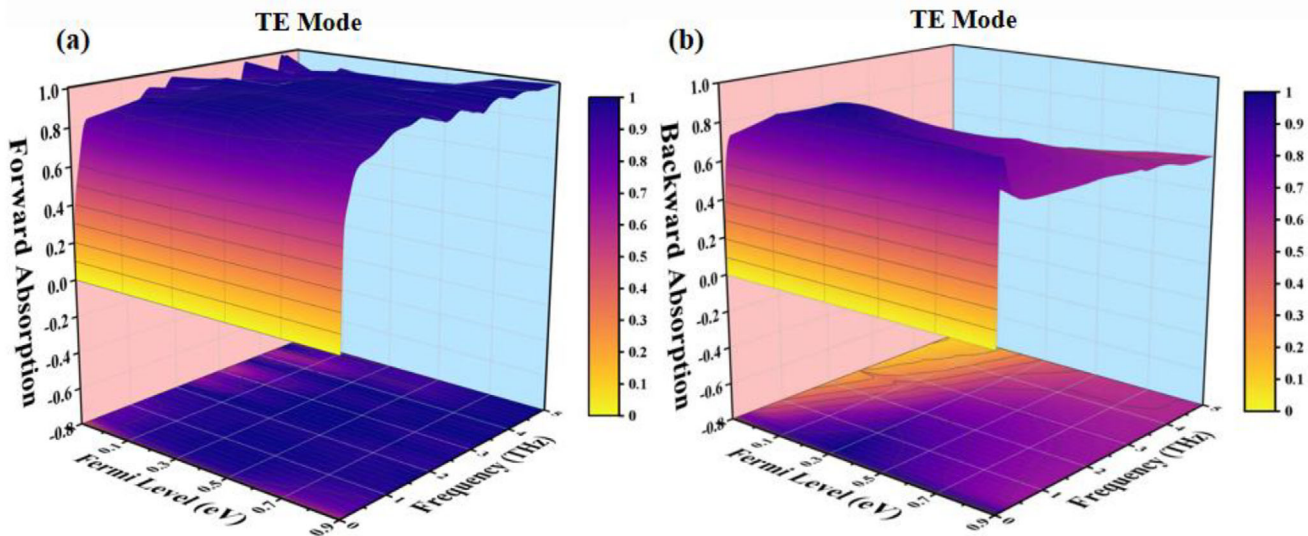


Figure 9. Variation of the absorption with E_f changing from 0 eV to 0.9 eV in the TE mode: a) the absorption when EM waves propagate forward, b) the absorption when EM waves propagate backward.

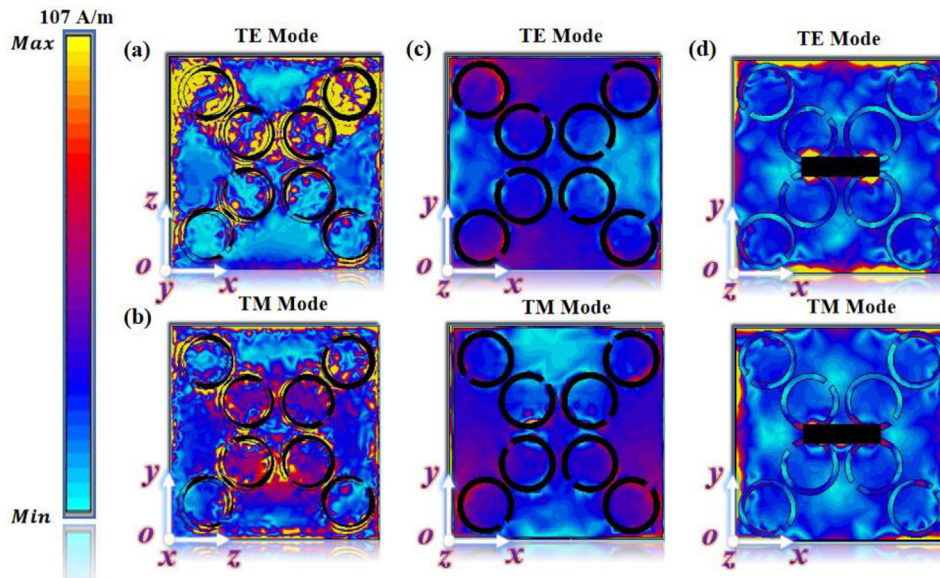


Figure 10. Surface current distributions of ($E_f = 0$ eV): a) the ORGS perpendicular to the y -axis at f_2 , b) the ORGS perpendicular to the x -axis at f_2 , c) the ORGM at f_2 , d) the RSG at f_2 .

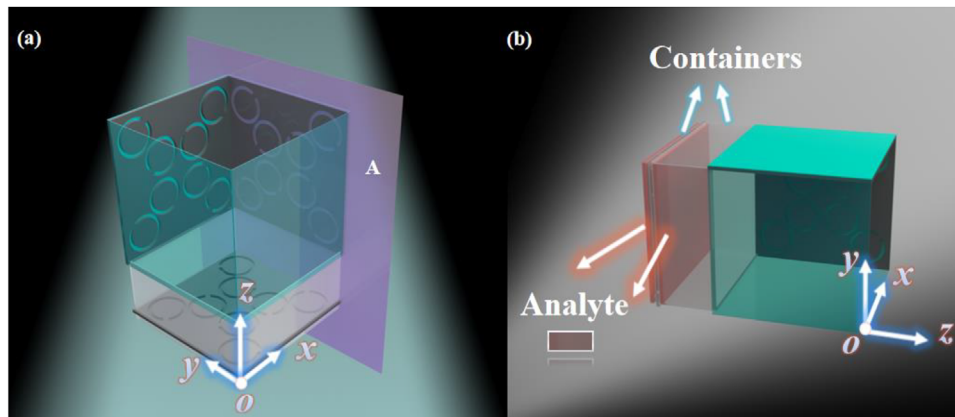


Figure 11. a) Schematic diagram of cross-section A, b) the view of the position of the analyte and containers.

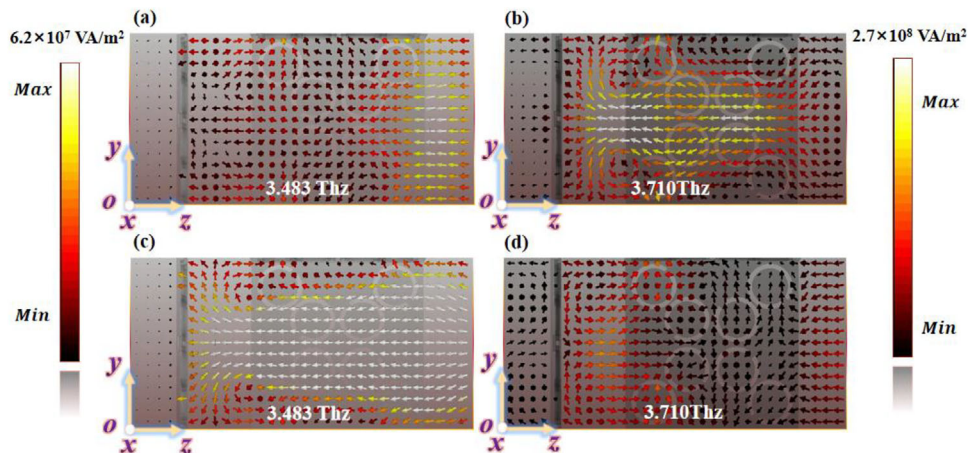


Figure 12. The power flow normalized results at the auxiliary plane A (depicted in purple) perpendicular to the x -axis: a) at 3.483 THz under forward direction. b) at 3.710 THz under forward direction. c) at 3.483 THz under backward direction. d) at 3.710 THz under backward direction.

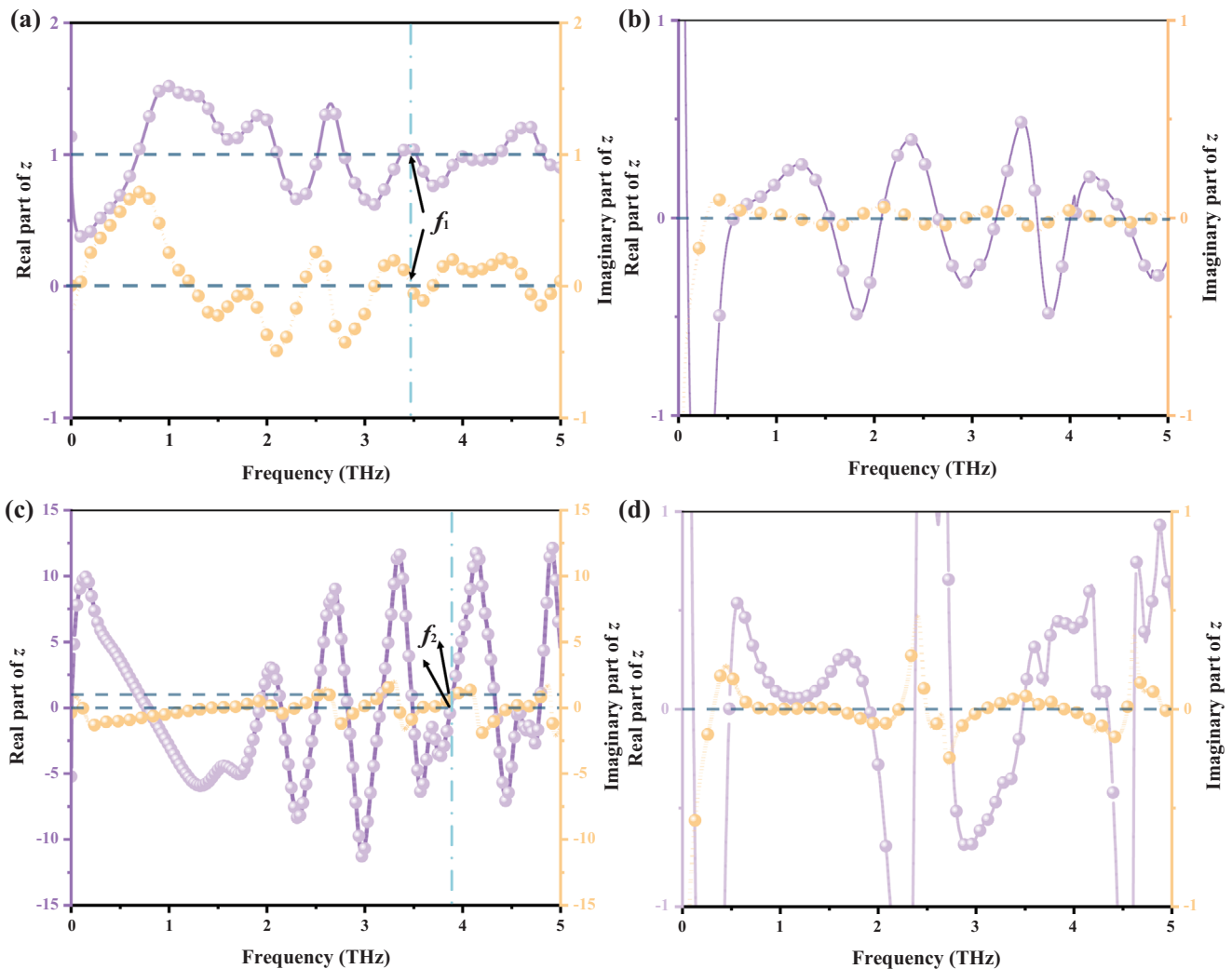


Figure 13. Normalized equivalent surface impedance curves for real and imaginary parts with frequency: a) in the forward direction ($E_f = 0.9$ eV), b) in the backward direction ($E_f = 0.9$ eV), c) in the forward direction ($E_f = 0$ eV), d) in the backward direction ($E_f = 0$ eV).

supplement the working principle of the Janus MS absorber. In the case of TE waves being normally incident, the complex normalized equivalent surface impedance of the MS is shown in **Figure 13**. It can be observed that when E_f is 0.9 eV, within the absorption band of the MS (0.754 ~ 5 THz) in the $-z$ -direction, the real and imaginary parts of the normalized equivalent surface impedance are close to 1 and 0, respectively. This is particularly evident at the perfect absorption frequency point f_1 , which indicates that the MS can effectively match the impedance of free space within the absorption frequency range, thereby achieving localization of EM energy and significantly improving absorption efficiency. Conversely, a considerable deviation from 1 in the real component of the equivalent surface impedance during absorption in the $+z$ -direction signifies a lower degree of impedance matching between the metasurface and free space, resulting in diminished backward absorption. In the case of $E_f = 0$ eV, a substantial disparity between the real component of the normalized equivalent surface impedance and 1 is observed for forward incident EM waves. Nevertheless, at the perfect absorption point

f_2 , the real part of the normalized equivalent surface impedance still tends toward 1, accompanied by an imaginary component approaching 0. When the EM waves are backward incident, both the real and imaginary parts of the normalized equivalent surface impedance undergo a significant change, indicating a mismatch with free space impedance, ultimately leading to reduced absorption.

2.3. The Mechanistic Analysis for Sensing

When $E_f = 0$ eV, an intriguing finding is the presence of a remarkable sensing characteristic at the perfect absorption point f_2 . Upon introducing the analyte in the containers, as depicted in **Figure 11b**, we discovered that the structure demonstrates favorable frequency shift properties with changes in the external n . As shown in **Figure 14**, when the n of the analyte changes from 1 to 1.5, a corresponding shift in frequency in the forward and backward directions occurred. By further investigation, it can

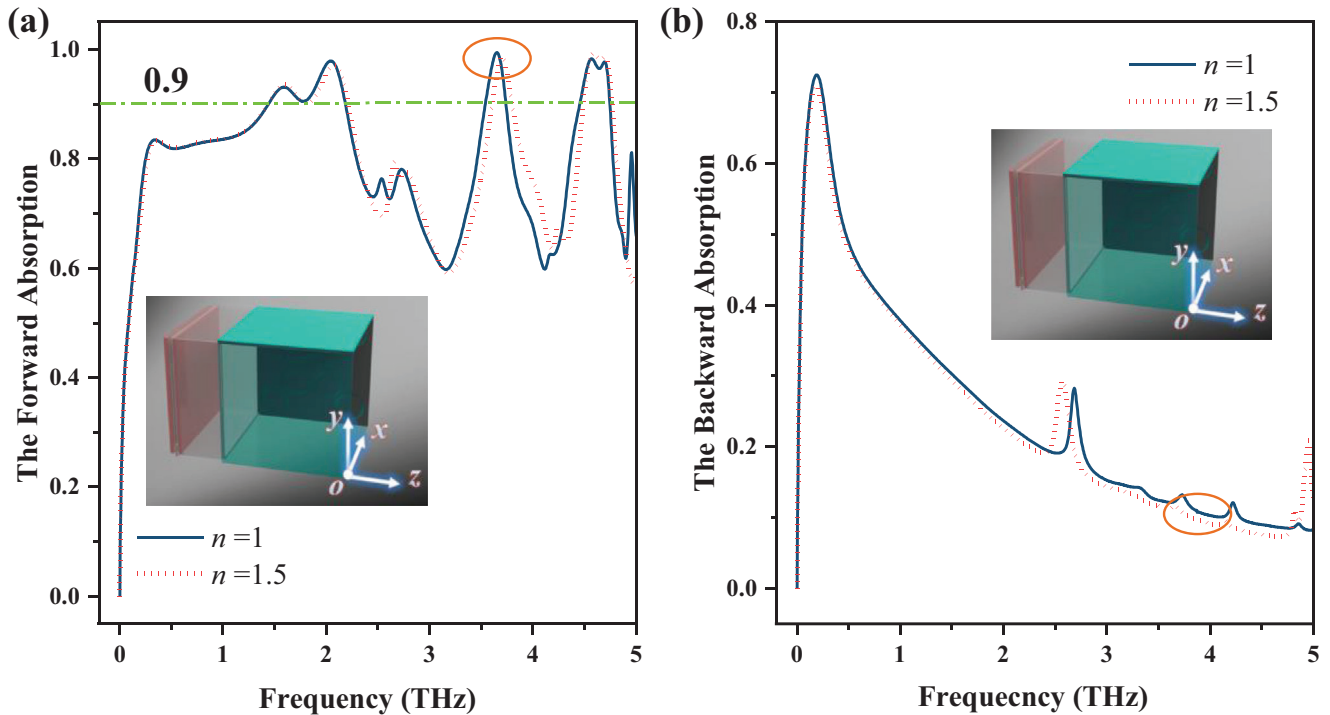


Figure 14. Absorption curves for n vary from 1 to 1.5: a) the absorption when EM waves propagate forward, b) the absorption when EM waves propagate backward.

be observed that as the n varies from 1.2 to 2.6, the absorption peak points are 3.6830, 3.6654, 3.6404, 3.6128, 3.5813, 3.5455, 3.5075, and 3.4786 THz in **Figure 15a**, showing an overall redshift phenomenon. Notably, the backward absorption at each frequency point also undergoes distinct changes in **Figure 15b**. By calculating the ΔA , we determined the corresponding absorption intensity differences to be 0.86227, 0.87325, 0.88262, 0.89045, 0.90257, 0.91038, 0.91792, and 0.92464. This excellent sensing performance is also evident in the refractive index range of 4.6 to 4.7. As shown in **Figure 15c,d**, when the n changes within this range, the absorption peak points are 3.2789, 3.2754, 3.2695, 3.2650, and 3.2611 THz, and the ΔA corresponds to 0.94161, 0.94314, 0.94479, 0.94592, and 0.94780.

It can be observed that ΔA at resonance displays a notable linear positive correlation with increasing n . By linear fitting and calculation, the results shown in **Figure 16a** were obtained when the n varied between 1.2 and 2.6 with an interval of 0.2, yielding an R^2 value of 0.9948. The high R^2 value indicates a good linearity, which is advantageous for the design of optical detectors. Similarly, when the n varied between 4.5 and 4.7 with an interval of 0.05, the calculated R^2 value was 0.99592, as demonstrated in **Figure 16b**.

When evaluating a detector, it is crucial to consider S , and a detector with superior performance will naturally have higher S . The definition of S is as follows:^[54,55]

$$S_1 = \frac{\Delta f}{\Delta n} \quad (17)$$

where Δf refers to the corresponding frequency shift when the n changes. By calculation, the S_1 corresponding to the two measurement ranges are 0.125 THz/RIU and 0.094 THz/RIU.

Based on our proposed MS, we innovatively introduce the difference detection as another method to calculate the S . That is to say, detector application is capable to be attained by the characteristic of the variation of ΔA with the changing n . Thus the S can be calculated using the following equation:

$$S_2 = \frac{\Delta A}{\Delta n} \quad (18)$$

As shown in **Figure 16**, the S_2 corresponding to the two n ranges are 0.0450 and 0.0304, respectively. It has to be admitted that the S of our MS is relatively low, but our novel point in the detection mechanism, through the absorption difference in the forward and backward directions for sensing detection, can better reduce the detection error. To emphasize the distinction between the MS and the traditional detectors, **Table 2** gives the performance indicators for comparison.^[56–60]

2.4. Parameter Discussion

Meanwhile, the separation distance h_1 between the square cavity and the intermediate structure emerges as a pivotal factor influencing the performance of this MS. **Figure 17a,b** depicts the profiles illustrating the variations in absorption with respect to h_1 when EM waves are incident in the forward and backward directions. Notably, the absorption performance of this structure

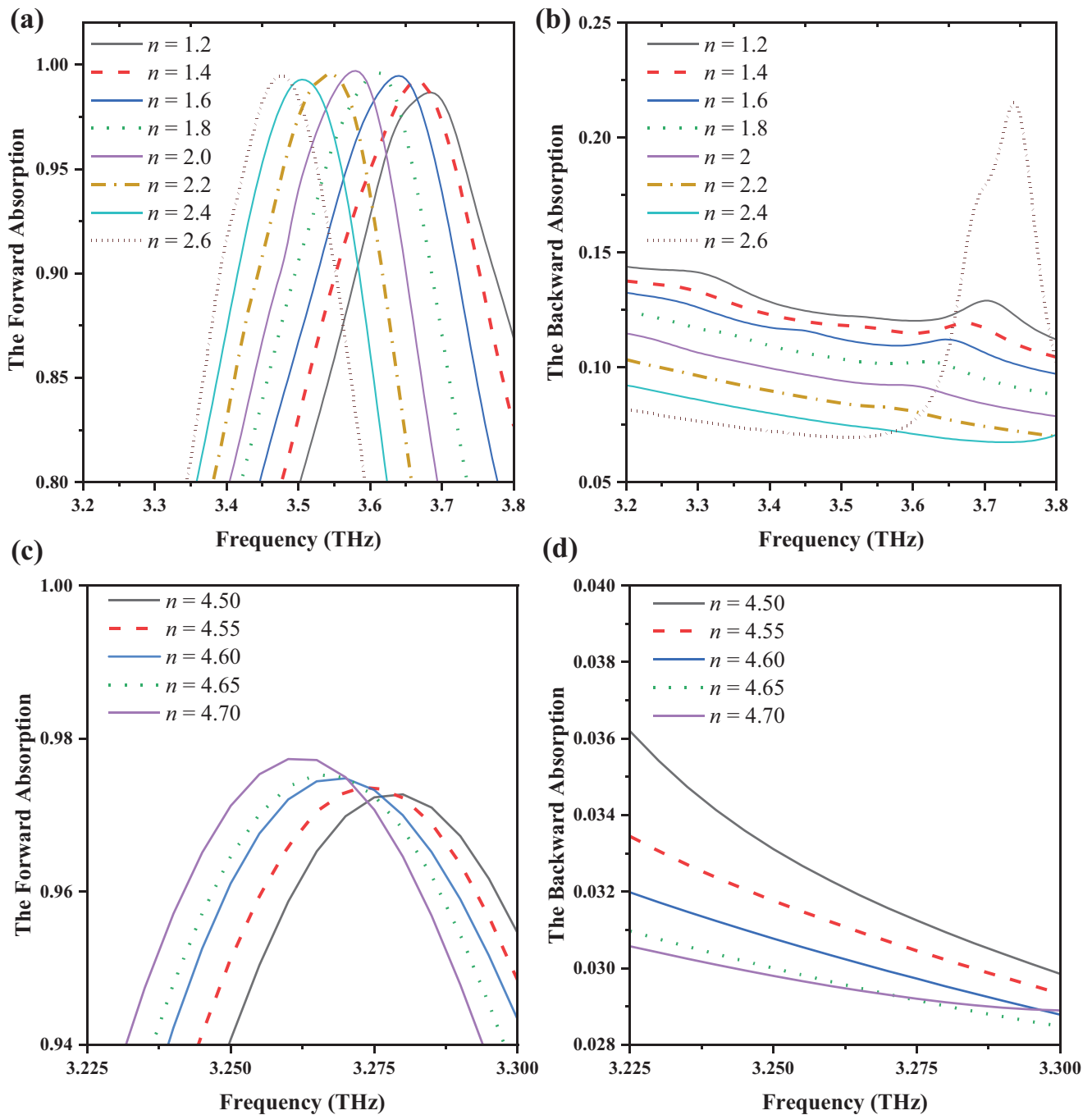


Figure 15. Graphs of absorption curves for n varying from 1.2 ~ 2.6 ($E_f = 0$ eV): a) the absorption in the forward direction, b) the absorption in the backward direction. Graphs of absorption curves for n varying from 4.5 ~ 4.7 ($E_f = 0$ eV): c) the absorption in the forward direction, d) the absorption in the backward direction.

exhibits a gradual decline in the $-z$ -direction as h_1 increases, accompanied by an escalating fluctuation in the absorption values within the frequency range of 1 to 3.5 THz. Conversely, analyzing the absorption in the $+z$ -direction reveals that the lowest absorption occurs at an h_1 value of $45 \mu\text{m}$, thereby resulting in a notable disparity between A_- and A_+ . Evidently, h_1 governs the coupling strength between the square cavity and the intermediate

structure, with the optimal distance representing an optimized parameter.

To provide a better representation of real-world applications, we further investigated the absorption characteristics of the structure at different θ in **Figure 18**. It was found that in the TE mode, the absorption in the forward direction remains relatively stable for θ below 60 degrees but starts to deteriorate above

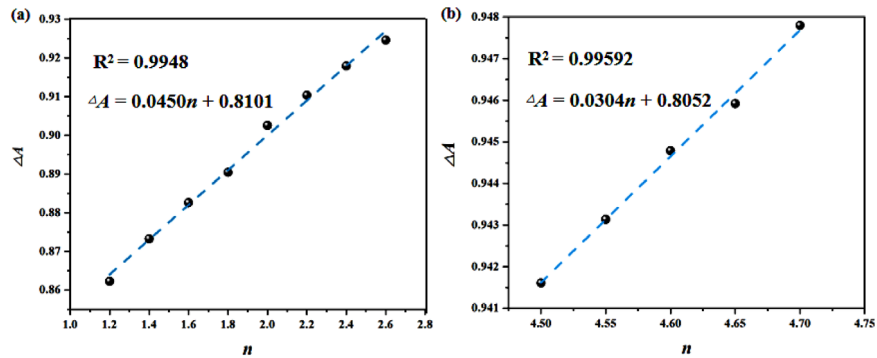


Figure 16. a) The linear relationship between the ΔA corresponds to n ranging from 1.2 ~ 2.6 at equal intervals of 0.2. b) The linear relationship between the ΔA corresponds to n ranging from 4.5 ~ 4.7 at equal intervals of 0.05.

Table 2. Comparison with other works.

Refs.	Function	Operating frequency	The measurement range of n and S	Control measure	Physical mechanism	Nonreciprocity
[56]	Sensing for identifying concentrations of glucose	Absorption: 0.5 ~ 1.8 THz	n : 1.1 ~ 1.6 S : 930.4 GHz/RIU	The size of the structure	Not difference detection	No
[57]	Sensing for n	0.1 ~ 0.5 THz	n : 1.2 ~ 2.0 S : 1.22 and 0.52 THz/(mol/L)	/	Not difference detection	No
[58]	Plasmon-induced transparency	1.5 ~ 4 THz	n : 1.32 ~ 1.40 S : 1.1 THz/RIU	Voltage, the polarization direction of the incident wave	Not difference detection	No
[59]	Sensing of nanometer scale thin analyte	0.8 ~ 1.2 THz	n : 1 ~ 1.5 S : 280 GHz/RIU	/	Not difference detection	No
[60]	Sensing for n	2 ~ 6 THz	n : 1 ~ 1.6 S : 851 GHz/RIU	Voltage	Not difference detection	No
This work	Detector for n , ultra-wideband absorber, Janus MS feature	Absorption: 0.754 ~ 5 THz	n : 1.2 ~ 2.6 and 4.5 ~ 4.7 S_1 = 0.125 and 0.094 THz/RIU S_2 = 0.0450 and 0.0304	Voltage, direction of the incident wave	Difference detection	Yes

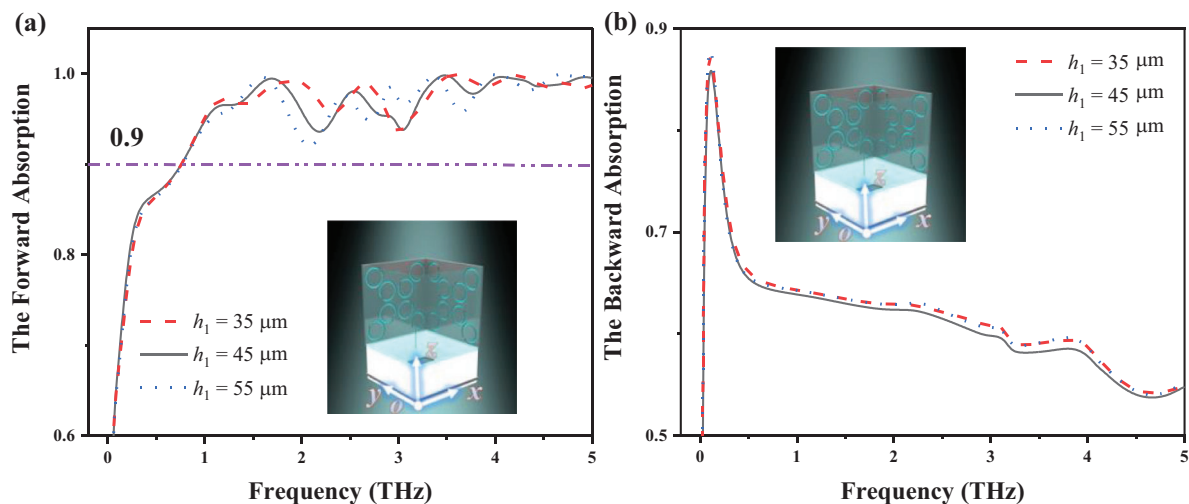


Figure 17. The absorption curves when h_1 varies from 35 μm to 55 μm ($E_f = 0.9$ eV): a) the absorption when EM waves are incident in the forward direction, b) the absorption when EM waves are incident in the backward direction.

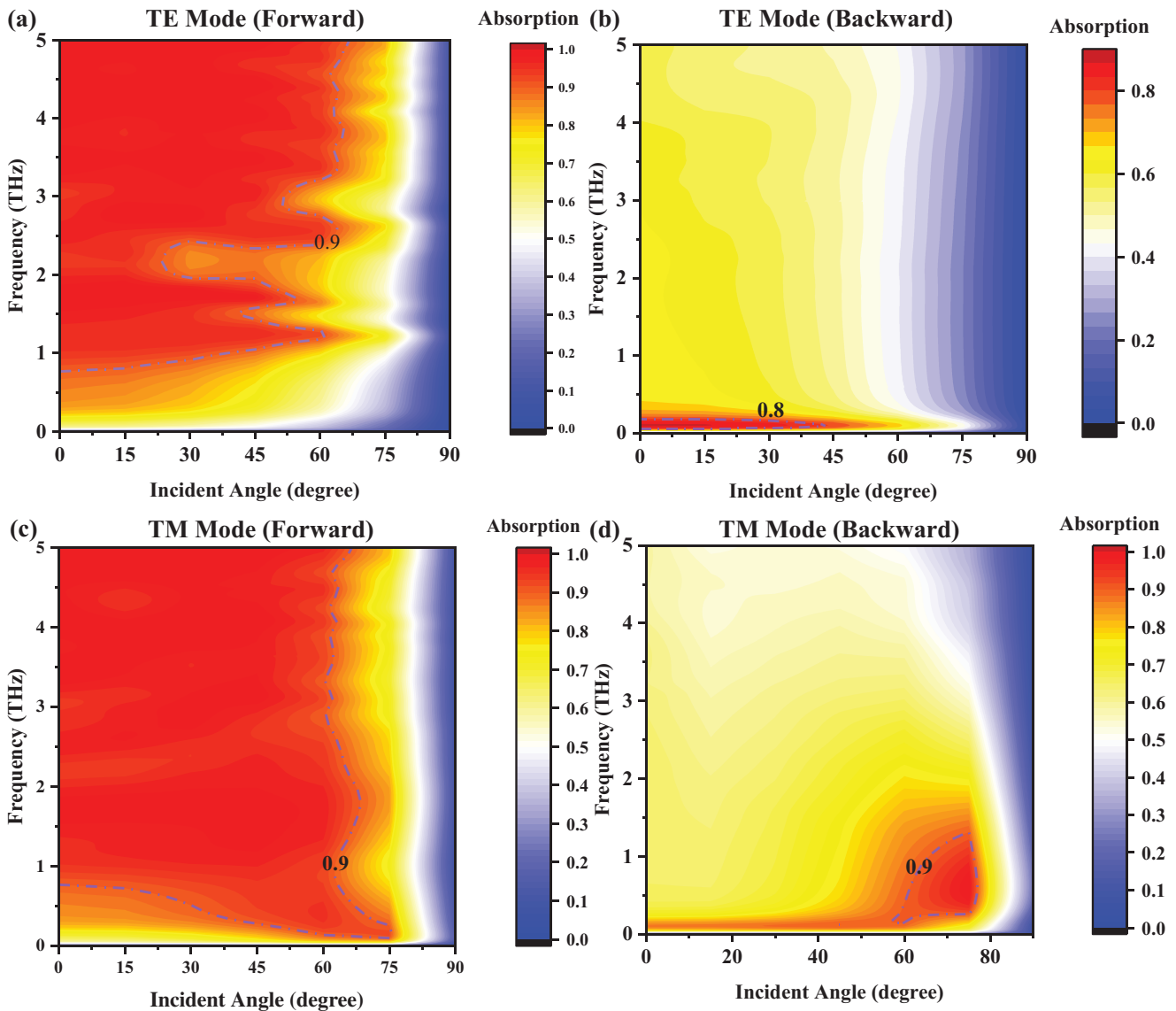


Figure 18. Absorption characteristics at different θ as EM waves propagate forward ($E_f = 0.9$ eV): a) in the TE mode, c) in the TM mode. Absorption characteristics at different θ as EM waves propagate backward ($E_f = 0.9$ eV): b) in the TE mode, d) in the TM mode.

60 degrees as displayed in Figure 18a. Conversely, the absorption in the backward exhibits a significant decrease when the θ exceeds 45 degrees in Figure 18b, and the ΔA gradually decreases. Notably, in the TM mode, this structure maintains excellent angular stability within the $0 \sim 60$ degrees θ range, achieving stable absorption with a value above 0.9 for a broadband range of 0.754 ~ 5 THz as the EM waves propagate forward. However, when the θ approaches 90 degrees, it achieves ultra-broadband absorption below 0.1.

We can interpret this phenomenon in this way, the RGS is polarization selective and TE waves are reflected, while TM waves can transmit through it. Thus TE waves cannot form plasma resonance, resulting in absorptivity is less than TM waves at a large θ . Within a specific range of θ , the excitation of plasmon resonances greatly localizes the EM wave energy, leading to high absorption values in TM mode. But when the angle approaches

90 degrees, the plasmonic resonance is disrupted, resulting in a sharp decrease in absorption. By observing the electric field and magnetic field distributions of RSG, we can find that when the θ is 89 degrees, its magnetic field and electric field intensity are greatly weakened compared with the case of $\theta = 0$ degree in Figure 19. Hence, the absorption characteristics of this structure can be well-tuned by adjusting the θ . Interestingly, in the TM mode, when the θ is between 60 and 80 degrees, the backward absorption shows a significant increase in absorption values from 0.5 THz to 1.5 THz. Specifically, at a θ of 75 degrees, a high absorption value of 0.998 can be achieved at 0.57 THz owing to the polarization selectivity of the RSG. In summary, this structure exhibits excellent angular stability and strong adaptability for practical applications.

The evaluation of the design's performance critically relies on its sensitivity to the ϕ of the incident EM wave. Consequently,

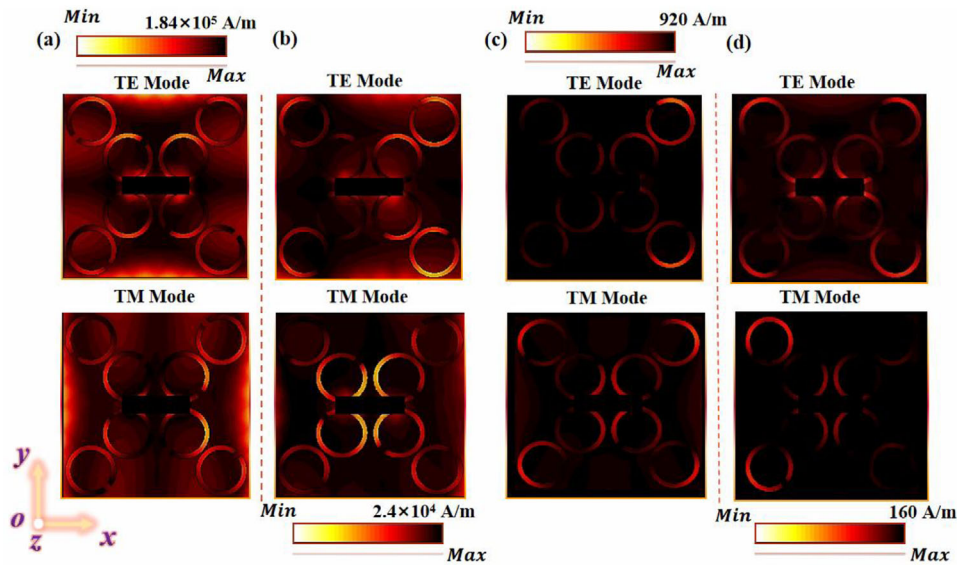


Figure 19. The electric field distribution of the RGS at different θ : a) $\theta = 0$ degree, b) $\theta = 89$ degrees. The magnetic field distribution of the RGS at different θ : c) $\theta = 0$ degree, d) $\theta = 89$ degrees.

it is crucial to assess the absorption efficiency of the MS under forward vertical incidence with various polarizations, as depicted in Figure 20. It can be clearly observed that with $E_f = 0.9$ eV, the absorption as well as the efficiency of the MS remain stable as the ϕ of the incident EM wave increases. This compellingly indicates that the structure exhibits insensitivity to the polarization characteristics of the incident EM wave. The insensitivity arises since when EM waves with different polarizations are vertically incident, their vector electric fields can always be decomposed into E_x and E_z components along the x and y directions, respectively. These components can induce resonances in the circular apertures parallel to the x -axis and y -axis, thereby localizing the EM wave components propagating in the two orthogonal direc-

tions. This enhances the EM density within the unit structure and increases the EM energy dissipation. Therefore, the characteristics of the MS are not affected by the polarization properties of the incident EM wave.

Moreover, we have to recognize that in the testing process, our experimental results will be affected by a lot of factors. Problems encountered in the measurement process, such as calibration errors in the device, difficulty in eliminating stray waves, and the effect of frequency differences in the THz source, making the results distorted. In addition, the results will be different when no plane waves are incident. We also find it hard to ensure that the analyte remains horizontal and unbent when the incident wave is incident at a specific angle. Due to the influence of gravity on

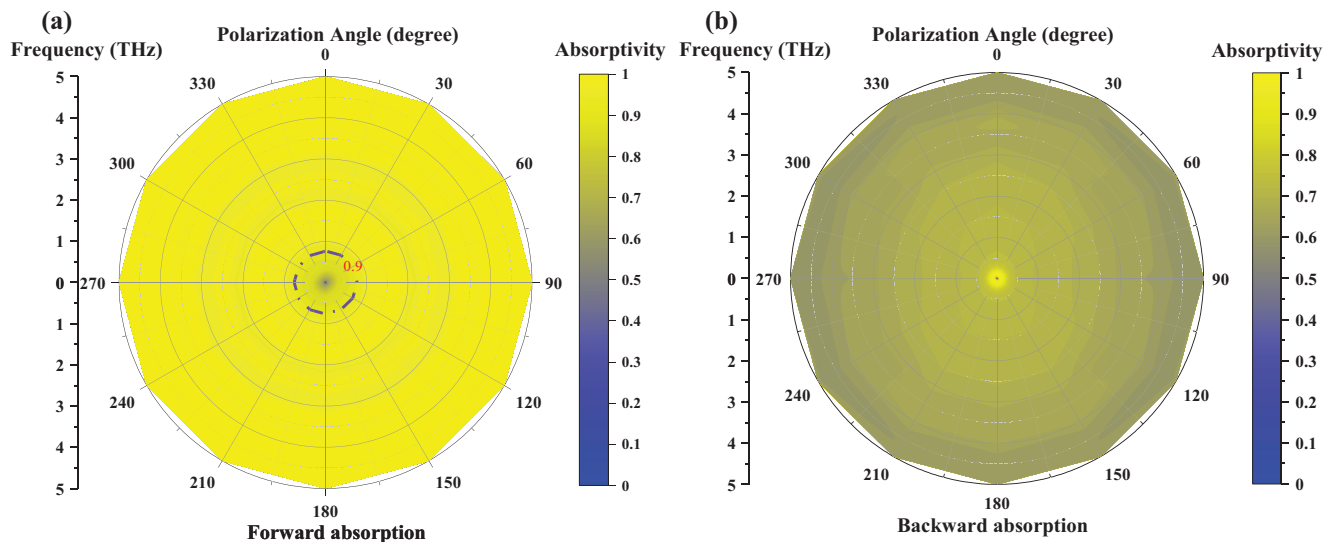


Figure 20. Absorption characteristics at various ϕ varying from $0 \sim 360$ degrees ($E_f = 0.9$ eV): a) the absorption when EM waves propagate forward, b) the absorption when EM waves propagate backward.

the structure, there will be a slight mechanical bending. When it comes to processing errors, this can lead to inhomogeneity of the parameters of the medium, as a homogeneous medium does not exist during implementation. There are nonlinearities and anisotropic differences, all of which can end up affecting the results.

3. Conclusion

In summary, this study introduces an innovative Janus detector employing the anapole mode, which demonstrates highly efficient absorption in the THz range by harnessing the tunable characteristics of graphene. The MS exhibits distinct frequency-selective effects in the forward and backward propagation directions. Particularly, when setting E_f to 0.9 eV, the proposed structure achieves ultra-broadband absorption exceeding 0.9 from 0.754 to 5 THz with a relative bandwidth of 147.6 %, in which the exceptional absorption rates surpass 98% within the range of 3.24 to 5 THz in the forward direction. In the case of the backward direction, the absorption remains around 0.6 within the 0.7 ~ 5 THz range, indicating a notable discrepancy in absorption between the $-z$ -direction and $+z$ -direction. Moreover, within the frequency range of 4.49 to 4.76 THz, the ΔA exceeds 0.9 as E_f is set to 0 eV. And the MS is capable of refractive index sensing at ≈ 3.71 THz in the condition of $E_f = 0$ eV. The investigation reveals that the MS can measure refractive indices within two ranges: 1.2 ~ 2.6 and 4.5 ~ 4.7, exhibiting sensitivities of 0.0450 and 0.0304, respectively. In addition, the MS demonstrates remarkable angular stability as the θ varies from 0 to 60 degrees in the TM mode and equipped with fabulous polarization-insensitive properties. In addition to THz applications, the structure can also be extended to other wavelength regions, such as the microwave and even optical range.^[61–63] All in all, the principles are analyzed by magnetic and electric fields, the scattering power intensity of multipole moments, energy flow and the absorption. This proposal holds significant potential for biomedical sensing, EM shielding, and comprehensive EM wave control.

Acknowledgements

This work was supported by the College Student Innovation Training Program of Nanjing University of Posts and Telecommunications.

Conflict of Interest

The authors declare no conflict of interest.

Data Availability Statement

The data that support the findings of this study are available from the corresponding author upon reasonable request.

Keywords

anapole mode, detectors, graphene, Janus metastructures, ultra-wideband absorption

Received: May 27, 2023
Revised: August 15, 2023
Published online:

- [1] P. H. Siegel, *IEEE Trans Microw Theory Tech* **2002**, *50*, 910.
- [2] A. Redo-Sanchez, X. C. Zhang, *IEEE J. Sel. Top. Quantum Electron.* **2008**, *14*, 260.
- [3] B. Ferguson, X. C. Zhang, *Nat. Mater.* **2002**, *1*, 26.
- [4] Y. Shi, Q. Zhou, C. Zhang, B. Jin, *Appl. Phys. Lett.* **2008**, *93*, 121115.
- [5] T. Dekorsy, H. Auer, C. Waschke, H. J. Bakker, H. G. Roskos, H. Kurz, *Phys. Rev. Lett.* **1995**, *74*, 738.
- [6] Y. Wang, F. Qi, Z. Liu, P. Liu, W. Li, H. Wu, W. Ning, *IEEE Trans. Terahertz Sci. Technol.* **2019**, *9*, 155.
- [7] J. Shi, Y. Wang, D. Xu, C. Yan, T. Chen, Y. He, J. Yao, *IEEE J. Sel. Top. Quantum Electron.* **2017**, *23*, 6800107.
- [8] E. Pickwell, V. P. Wallace, *J. Phys. D: Appl. Phys.* **2006**, *39*, R301.
- [9] Y. Wang, F. Qi, Z. Liu, P. Liu, W. Li, H. Wu, W. Ning, *IEEE Trans Terahertz Sci Technol* **2019**, *9*, 155.
- [10] J. Shi, Y. Wang, D. Xu, C. Yan, T. Chen, Y. He, J. Yao, *IEEE J. Sel. Top. Quantum Electron.* **2017**, *23*, 6800107.
- [11] R. Chhantyal-Pun, A. Valavanis, J. T. Keeley, P. Rubino, I. Kundu, Y. Han, E. H. Linfield, *Opt. Lett.* **2018**, *43*, 2225.
- [12] G. Tzdydnzhapov, P. Gusikhin, V. Muravev, A. Dremin, Y. Nefyodov, I. Kukushkin, *J. Infrared Millim. Terahertz Waves* **2020**, *41*, 632.
- [13] H. J. Song, T. Nagatsuma, *IEEE Trans. Terahertz Sci. Technol.* **2011**, *1*, 256.
- [14] D. R. Smith, J. B. Pendry, M. C. K. Wiltshire, *Science* **2004**, *305*, 788.
- [15] T. C. Edwards, M. B. Steer, *Mater. Sci. Eng. B* **2006**, *178*, 1285.
- [16] Y. P. Yang, D. Q. Xu, W. L. Zhang, *Opt. Express* **2018**, *26*, 31589.
- [17] M. Yang, L. Liang, Z. Zhang, Y. Xin, D. Wei, X. Song, H. Zhang, Y. Lu, M. Wang, M. Zhang, *Opt. Express* **2019**, *27*, 19520.
- [18] V. P. Gusynin, S. G. Sharapov, J. P. Carbotte, *J. Phys.: Condens. Matter* **2007**, *19*, 20.
- [19] J. Chen, M. Badioli, P. Alonso-González, S. Thongrattanasiri, F. Huth, J. Osmond, M. Spasenović, A. Centeno, P. Godignon, A. Z. Elorza, N. Camara, F. J. G. de Abajo, R. Hillenbrand, F. H. L. Koppens, *Nature* **2012**, *487*, 77.
- [20] F. Bonaccorso, Z. Sun, T. Hasan & A. C. Ferrari, *Nat. Photonics* **2010**, *4*, 611.
- [21] X. Chen, W. Fan, H. Song, *Carbon* **2018**, *133*, 416.
- [22] B. Zhang, Y. Qi, T. Zhang, Y. Zhang, W. Liu, L. Wang, J. Ding, X. Wang, Z. Yi, *Results Phys.* **2021**, *25*, 104233.
- [23] Y. B. Zel'dovich, *Sov. Phys. JETP* **1958**, *6*, 1186.
- [24] N. Papisimakis, V. A. Fedotov, V. Savinov, T. A. Raybould, N. I. Zheludev, *Nat Mater* **2016**, *15*, 263.
- [25] L. Y. Guo, X. H. Ma, Z. Q. Chang, C. L. Xu, J. Liao, R. Zhang, *J Mater Res Technol* **2021**, *14*, 772.
- [26] P. Yang, Y. Ding, Z. Lin, Z. Chen, Y. Li, P. Qiang, M. Ebrahimi, W. Mai, C. P. Wong, Z. L. Wang, *Nano Lett.* **2014**, *14*, 731.
- [27] H. C. Yang, J. Hou, V. Chen, Z. K. Xu, *Angew. Chem., Int. Ed.* **2016**, *55*, 13398.
- [28] X. Pang, C. Wan, M. Wang, Z. Lin, *Angew. Chem., Int. Ed.* **2014**, *53*, 5524.
- [29] Y. Yi, L. Sanchez, Y. Gao, Y. Yu, *Analyst* **2016**, *141*, 3526.
- [30] L. Zhao, L. Pan, K. Zhang, S. Guo, W. Liu, Y. Wang, Y. Chen, X. Zhao, H. Chan, *Lab Chip* **2009**, *9*, 2981.
- [31] H. Xie, Z. G. She, S. Wang, G. Sharma, J. W. Smith, *Langmuir* **2012**, *28*, 4459.
- [32] A. Walther, A. H. Muller, *Chem. Rev.* **2013**, *113*, 5194.
- [33] Q. Cheng, M. Li, Y. Zheng, B. Su, S. Wang, L. Jiang, *Soft Matter* **2011**, *7*, 5948.
- [34] B. Yue, B. Zhang, J. You, Y. Li, L. Li, J. Li, *RSC Adv.* **2016**, *6*, 17215.
- [35] H. Yi, S. W. Qu, K. B. Ng, C. K. Wong, C. H. Chan, *IEEE Trans Antennas Propag* **2017**, *66*, 209.
- [36] T. Cai, G. Wang, S. Tang, H. Xu, J. Duan, H. Guo, F. Guan, S. Sun, Q. He, L. Zhou, *Phys. Rev. Appl.* **2017**, *8*, 034033.
- [37] L. Zhang, R. Y. Wu, G. D. Bai, H. T. Wu, Q. Ma, X. Q. Chen, T. J. Cui, *Adv. Funct. Mater.* **2018**, *28*, 1802205.

- [38] G. Shang, G. Hu, C. Guan, Y. Wang, K. Zhang, Q. Wu, J. Liu, X.-M. Ding, S. N. Burokur, H. Li, *Nanophotonics* **2022**, *11*, 3729.
- [39] X. Wang, H. Wang, J. Wang, X. Liu, H. Hao, Y. S. Tan, Y. Zhang, H. Zhang, X. Ding, W. Zhao, *Nat. Commun.* **2023**, *14*, 2063.
- [40] Z. Zhao, Y. Wang, C. Guan, K. Zhang, Q. Wu, H. Li, J. Liu, S. N. Burokur, X. Ding, *Photonix* **2022**, *3*, 15.
- [41] S. Yuan, R. Yang, J. Tian, W. Zhang, *Int. J. RF Microw. Comput.-Aided Eng.* **2020**, *30*, 22014.
- [42] Q. Y. Wen, H. W. Zhang, Y. S. Xie, Q. H. Yang, Y. L. Liu, *Appl. Phys. Lett.* **2009**, *95*, 241111.
- [43] M. Changwei, M. Wenying, T. Yi, T. Yuzhu, *Guangdian Gongcheng* **2018**, *45*, 180298.
- [44] G. W. Hanson, *J. Appl. Phys.* **2008**, *103*, 064302.
- [45] X. Huang, W. He, F. Yang, J. Ran, B. Gao, W. L. Zhang, *Opt. Express* **2018**, *26*, 25558.
- [46] H. Yan, X. Li, B. Chandra, G. Tulevski, Y. Wu, M. Freitag, W. Zhu, P. Avouris, F. Xia, *Nat. Nanotechnol.* **2012**, *7*, 330.
- [47] A. C. Tasolamprou, A. D. Koulouklidis, C. Daskalaki, C. P. Mavidis, G. Kenanakis, G. Deligeorgis, Z. Viskadourakis, P. Kuzhir, S. Tzortzakis, M. Kafesaki, *ACS Photonics* **2019**, *6*, 720.
- [48] M. Konishi, T. Morita, T. Fukuoka, T. Imura, K. Kakugawa, D. Kitamoto, *Appl. Microbiol. Biotechnol.* **2007**, *75*, 521.
- [49] Y. Cheng, H. Chen, J. Zhao, X. Mao, Z. Cheng, *Opt. Mater. Express* **2018**, *8*, 1399.
- [50] E. Economou, *Phys. Rev.* **1969**, *182*, 539.
- [51] A. A. Basharin, V. Chuguevsky, N. Volsky, M. Kafesaki, E. N. Economou, *Phys. Rev. B* **2017**, *95*, 035104.
- [52] Z. Li, K. Aydin, E. Ozbay, *Phys Rev E* **2009**, *79*, 026610.
- [53] L. L. Hou, J. Y. Chin, X. M. Yang, X. Q. Lin, R. Liu, F. Y. Xu, T. J. Cui, *J. Appl. Phys.* **2008**, *103*, 064904.
- [54] C. Fang, Y. Cheng, Z. He, J. Zhao, R. Gong, *Optik* **2017**, *137*, 148.
- [55] H. Ji, B. Zhang, G. Wang, W. Wang, J. Shen, *Opt. Commun.* **2018**, *412*, 37.
- [56] J. Yang, L. Qi, B. Li, L. Wu, D. Shi, J. A. Uqaili, X. Tao, *Results Phys.* **2021**, *26*, 104332.
- [57] P. Cao, Y. Wu, Z. Wang, Y. Li, J. Zhang, Q. Liu, L. Cheng, T. Niu, *IEEE Access* **2020**, *8*, 219525.
- [58] T. Chen, D. Liang, W. Jiang, *IEEE Sens. J.* **2022**, *22*, 14084.
- [59] Y. K. Srivastava, R. T. Ako, M. Gupta, M. Bhaskaran, S. Sriram, R. Singh, *Appl. Phys. Lett.* **2019**, *115*, 151105.
- [60] M. R. Nickpay, M. Danaie, A. Shahzadi, *Plasmonics* **2022**, *17*, 237.
- [61] Y. Zhu, L. Cao, A. Merkel, S. W. Fan, B. Vincent, B. Assouar, *Nat. Commun.* **2021**, *12*, 7089.
- [62] G. Shang, H. Li, Z. Wang, S. N. Burokur, K. Zhang, J. Liu, Q. Wu, X. Ding, X. Ding, *ACS Appl. Electron. Mater.* **2021**, *3*, 2638.
- [63] C. Wan, C. Dai, S. Wan, Z. Li, Y. Shi, Z. Li, *Opt. Express* **2021**, *29*, 33954.